Production of Hydrogen Using Nanocrystalline Protein-Templated Catalysts on M13 Phage

Brian Neltner,[†] Brian Peddie,[†] Alex Xu,[†] William Doenlen,[†] Keith Durand,[‡] Dong Soo Yun,[†] Scott Speakman,[†] Andrew Peterson,[§] and Angela Belcher[†,⊥,*]

[†]Department of Materials Science and Engineering, [‡]Department of Mechanical Engineering, [§]Department of Chemical Engineering, and [⊥]Department of Biological Engineering, Massachusetts Institute of Technology, Cambridge, Massachusetts 02139

ABSTRACT For decades, ethanol has been in use as a fuel for the storage of solar energy in an energy-dense, liquid form. Over the past decade, the ability to reform ethanol into hydrogen gas suitable for a fuel cell has drawn interest as a way to increase the efficiency of both vehicles and stand-alone power generators. Here we report the use of extremely small nanocrystalline materials to enhance the performance of 1% Rh/10% Ni@CeO_2 catalysts in the oxidative steam reforming of ethanol with a ratio of 1.7:1:10:11 (air/EtOH/water/argon) into hydrogen gas, achieving 100% conversion of ethanol at only 300 °C with 60% H_2 in the product stream and less than 0.5% CO. Additionally, nanocrystalline 10% Ni@CeO_2 was shown to achieve 100% conversion of ethanol at 400 °C with 73% H_2, 2% CO, and 2% CH_4 in the product stream. Finally, we demonstrate the use of biological templating on M13 to improve the resistance of this catalyst to deactivation over 52 h tests at high flow rates (120 000 h^{-1} GHSV) at 450 °C. This study suggests that the use of highly nanocrystalline, biotemplated catalysts to improve activity and stability is a promising route to significant gains over traditional catalyst manufacture methods.

KEYWORDS: ceria · catalyst · ethanol · fuel cell · hydrogen

Hydrogen fuel cells generate power by chemically converting hydrogen and oxygen into water. This process does not produce power through the use of a heat engine, so the maximum efficiency can be quite high.[1] Although hydrogen has a mass energy density of 141.8 MJ/kg, the volumetric energy density is only 0.0116 MJ/L for uncompressed hydrogen and only 11.4 MJ/L for hydrogen compressed to 100 MPa (not including the weight and volume of the tank required to maintain such a high pressure). By comparison, ethanol has an energy density of 29.7 MJ/kg but has a volumetric energy density of 23.4 MJ/L at atmospheric pressure.[2] By catalytically reforming ethanol into hydrogen gas, the benefits of having a high energy density fuel can be combined with the benefits of using hydrogen fuel cells to perform work more efficiently, resulting in a significantly more practical way to incorporate fuel cells into existing systems.

The catalytic oxidative steam reforming of ethanol−water mixtures saw a major breakthrough in 2004, when the complete conversion of ethanol over rhodium−ceria (Rh@CeO_2) catalysts was observed at 650 °C.[3] Since then, the conversion of ethanol into hydrogen gas over ceria (CeO_2) has been widely investigated and makes a good prototypical reaction to study the effects of biotemplating and nanocrystallinity on catalytic performance.[3−24] The overall oxidative steam reforming reaction is

$$C_2H_5OH + 2H_2O + 1/2O_2 \rightarrow 2CO_2 + 5H_2 \quad (1)$$

and is slightly exothermic with $\Delta H_R \sim -50$ kJ/mol, allowing for autothermal operation when combined with a limited amount of total combustion.[3] In this reaction, water is consumed, so the molar ratio of H/C in the product stream is not equal to the ratio found in ethanol (3:1).

Combining rhodium with nickel on CeO_2(Rh−Ni@CeO_2) enhances the ability of the catalyst to oxidatively steam reform ethanol, especially at low temperatures.[6,10] The presence of both nickel and rhodium allows for the efficient decomposition of ethanol to smaller molecules through C−C bond cleavage, as well as the conversion of methane, CO, and H_2O to H_2 and CO_2. Nickel alone tends to produce more acetaldehyde than the mixed system, and rhodium alone tends to produce large amounts of CO and CH_4 compared to the mixed system. Nickel is highly active in the steam reforming necessary to convert methane and methanol into hydrogen and carbon dioxide in the presence of water and also to allow for the water gas-shift reaction to convert residual carbon monoxide and water into hydrogen and carbon dioxide.[6,25]

*Address correspondence to belcher@mit.edu.

Received for review February 19, 2010 and accepted May 24, 2010.

Published online June 7, 2010.
10.1021/nn100346h

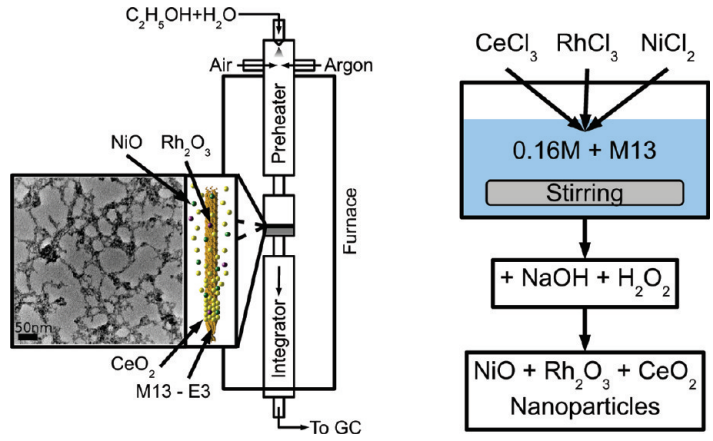

Figure 1. Experimental design. Rhodium, nickel, and ceria are simultaneously nucleated on the surface of the M13 phage, forming a highly porous structure. The resulting dried powders are tested in a custom-built chemical reactor to characterize the performance for hydrogen production from ethanol.

Metal clusters in contact with oxygen vacancies on the surface of CeO_2 are generally the most active sites for catalysis. Increasing surface area, oxygen vacancy concentration, and the number of metal cluster interactions is critical for catalytic efficiency.[5,6,25−33] If metal ions are allowed to form nanoparticles *via* traditional drying and calcining methods, the final position of nanoparticles is random on the surface, allowing for the migration of the active metal. Ceria particle size increases are associated with decreased oxygen vacancy concentrations and decreased overall activity, so extremely small, stable ceria particles are very important for maintaining long-term activity.[6,28−34]

The M13 bacteriophage is a filamentous bacteriophage which can be engineered to self-assemble nanowires through the modification of surface proteins, causing the coat to nucleate a variety of materials. These self-assembled structures have been shown to produce improved properties in a variety of applications.[35−38] In this work, we template nickel, rhodium, and ceria onto the surface of the M13 bacteriophage in order to produce catalysts with excellent dispersion, higher thermal stability, and a more porous structure than catalysts made using other methods.

RESULTS AND DISCUSSION

The effect of biotemplating on catalytic performance was investigated by using a variant of M13 where the major coat protein expresses the amino acid sequence AEEE on the surface of the phage. The major coat protein is expressed ~2700 times on the surface of the phage, so this results in ~8100 glutamic acid groups displayed on the surface which would otherwise be absent. At neutral pH, this surface is strongly negatively charged in comparison with a wild-type M13 phage.

The highly negative surface coat of the M13 phage attracts metal ions in solution and acts as a nucleation site for the formation of CeO_2 nanowires with nickel and rhodium impurities. The catalysts produced using this method were characterized using X-ray diffraction (XRD), transmission electron microscopy (TEM), BET surface area analysis, and energy-dispersive X-ray spectroscopy (EDS) in order to understand the relationship between structure and performance.

The catalysts produced with this process were loaded into a reactor (described in Figure S6, Supporting Information) held between 200 and 450 °C. The products produced by flowing ethanol and water over the catalyst were analyzed using gas chromatography (GC) as outlined in Figure 1.

Structure. Catalysts were grown by introducing the M13 variant into a solution of $CeCl_3$, $NiCl_2$, and $RhCl_3$. After equilibration for 30 min, the metal salts were hydrolyzed and partially oxidized using a mixture of NaOH and H_2O_2 in the presence of different concentrations of the mutant M13 phage. The M13 phage is viable for short times in pH as high as 11. However, in this case, where the phage is being used primarily as a template, it does not need to remain viable to successfully template wires. The powders produced using syntheses of this type also proceed extremely rapidly, often completing nucleation in seconds. Due to the rapid nucleation of particles, any instability of the phage due to the presence of NaOH does not damage the ability to form nanowires, and similar syntheses can be used to synthesize wires of RuO_2 and Mn_3O_4. However, in some cases, the presence of very large amounts of hydrogen peroxide was seen to break the virus-based wires into shorter rods of material.

TEM images of catalysts produced using biotemplating on M13 compared to untemplated catalyst show dramatic changes to the nanostructure at even fairly low concentrations of M13, as shown in Figure 2. After nucleation and precipitation, as described in the Experimental Section, the particles are heat treated at 400 °C in order to burn off residual phage, leaving a relatively clean catalyst, likely with some small amount of residual contamination of biologically common elements.

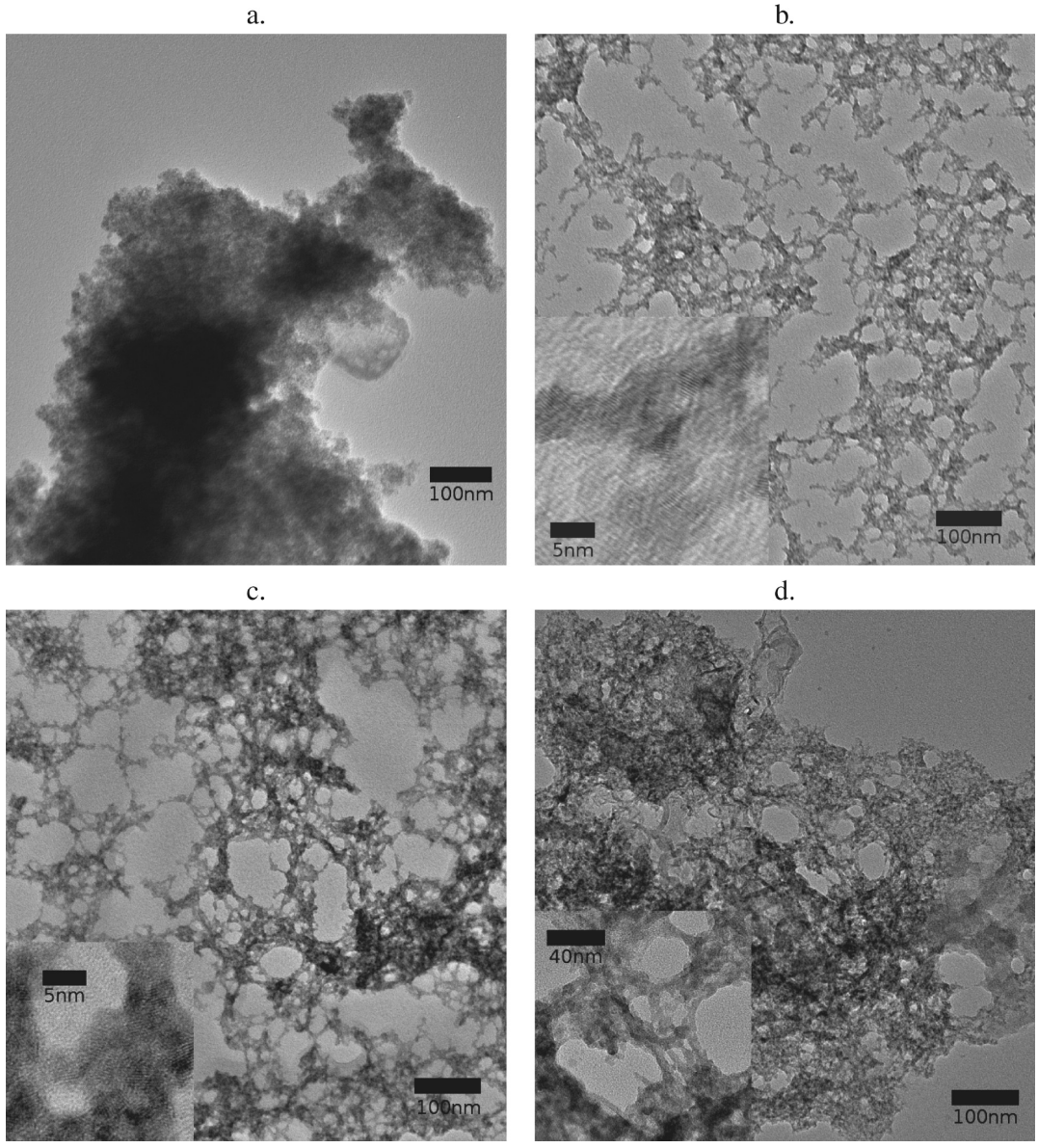

Figure 2. TEM images showing the effect of adding the AEEE M13 mutant bacteriophage on the microstructure of the catalyst. Catalyst made at 1 mM metal precursor, (a) without M13, (b) with 10^7 M13/mL, (c) with 10^{10} M13/mL, (d) with 10^{13} M13/mL. Insets show higher magnification images.

The catalyst nanostructure was further analyzed with BET (Figure S2, Supporting Information). BET pore size distribution measurements show a narrower pore size distribution, with 90% of pore area contained in pores less than 4.5 nm for M13-templated catalyst *versus* 5.9 nm for untemplated catalyst of identical composition. The total BET surface area for M13-templated catalyst was 180 m^2/g *versus* 143 m^2/g for untemplated catalyst of identical composition. This increased surface area shows that the templating process can be used to improve the total exposed surface area of materials formed *via* direct nucleation and precipitation. Additionally, the smaller pore size distribution could impact the selectivity of the catalyst for some reactions by physically inhibiting the accessibility of active sites to large molecules. The extreme example of this is in zeolites, which have nearly homogeneous pore sizes and exceptional selectivity.

Dispersion and Stability. XRD spectra were taken of samples made with and without M13, formed using an input molar concentration of 1:5:94 (Rh/Ni/Ce) immediately after drying and again after 60 h at 400 °C in air (Figure S3, Supporting Information). For both samples, only CeO_2 peaks were visible immediately after drying, indicating that rhodium and nickel phases are only present as amorphous, or extremely small, nanocrystals. After heat treatment, the sample made using M13 continued to show only CeO_2 peaks while the sample made without M13 began to show secondary peaks, suggesting that M13 encourages better incorporation of metal into the CeO_2 structure. The untemplated sample also shows larger crystallite growth than the

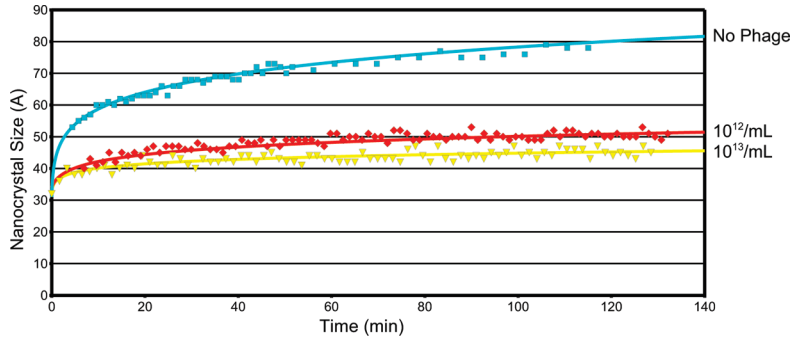

Figure 3. Thermal stability test of untemplated and M13-templated CeO_2 nanoparticles over 3 h at 500 °C in air. All particles were made at a 10 mM concentration of $CeCl_3$. From top to bottom, no M13 showing a growth exponent of 8, 10^{12} M13/mL showing a growth exponent of 13, and 10^{13} M13/mL showing a growth exponent of 21. This demonstrates that as more M13 is added the thermal stability of the CeO_2 crystallites improves.

M13-templated sample over the heat treatment, although the templated sample had a larger initial crystallite size.

To investigate the nanoscale elemental distribution using TEM, catalyst samples were heat treated at 400 °C for 2 h to remove any residual carbon and fully calcine the materials. Samples were resuspended in ethanol and deposited onto a TEM grid to examine the dispersion of rhodium and nickel into the ceria structure. In the case of both nanoparticles (Figure S4, Supporting Information) and nanowires (Figure S5, Supporting Information), the materials formed *via* this route appear to be well-dispersed and of approximately the elemental ratios predicted by the precursor fractions.

The nanowires formed with varying amounts of M13 phage for templating were analyzed for thermal stability by heating to 500 °C using an *in situ* furnace on the PANalytical X'Pert PRO diffractometer. Ceria crystallite size was estimated using the isolated {200} peak at 48°, with approximately 1 min time resolution between measurements of crystallite size. The resulting crystallite sizes measured over 2 h were fit using a power-law model of

$$D(t)^m - D(0)^m = kt \qquad (2)$$

where D is the average nanocrystal diameter, m is the growth exponent, k is the rate constant for sintering, and t is the time. This model showed suppression of ceria nanocrystal growth as more M13 is added during synthesis, with the growth exponent increasing from 8 with no M13 to 21 with 10^{13}/mL M13 and 10 mM metal precursor, as shown in Figure 3. The catalytic performance decreases as nanocrystallite size increases, making this improved thermal stability critical in creating a high-performance catalyst.[6,28,29,34]

Catalytic Tests. For catalytic tests, a premixed ethanol/water mixture was injected into a preheater using a fuel injector, where it was mixed with air and argon to keep the total flow rate of gas at ~200 mL/min in a molar ratio of 1.7:1:10:11 (air/ethanol/water/argon). The input stream was preheated to the reaction temperature and passed through a thin layer of catalyst of varying amounts between 100 and 1000 mg. The final output composition was sampled using a gas chromatography column. The results were used to calculate the concentrations of ethanol, water, nitrogen, oxygen, CO_2, H_2, CH_4, acetaldehyde, and CO with samples taken every 35 min. No other major products were detected.

Overall conversion was calculated as the ratio of ethanol consumed to ethanol injected, estimated using the amount of nitrogen detected as an internal standard along with the known molar ratio of nitrogen to ethanol at the inlet. The ratio of N_2 to ethanol at the inlet is 1.33:1 based on the total flow rate of air and ethanol, so the conversion is calculated as

$$\text{conv\%} = 1 - \frac{[\text{EtOH}]}{[N_2]/1.33} \qquad (3)$$

where [EtOH] is the measured molar amount of ethanol in the output stream and $[N_2]$ is the measured molar amount of nitrogen in the output stream.

Composition was calculated as the ratio of a given product to the total sum of products including only CO_2, H_2, CO, CH_4, and acetaldehyde

$$X\% = \frac{[X]}{\sum_i [i]} \qquad (4)$$

where X% is the calculated fraction for product X, and $[X]$ is the molar amount of product X. The fractions are then scaled down by

$$\bar{X}\% = X\% \times \text{Conv\%} \qquad (5)$$

for easier display in a stacked bar chart. Water is consumed during this reaction, so the molar ratio of hydrogen to carbon can vary depending on the amount of steam reforming that occurs. In experiments, the actual measured H/C ratio varied quite a bit, from as low as ~3:1 at low temperatures to ~6:1 at high temperatures.

Gas chromatography was used to take 36 samples over 21 h at temperatures ranging from 200 to 400 °C using 1000 mg of either M13-templated or untemplated catalyst (~12 000 h^{-1} GHSV). In both cases, complete conversion occurs at 300 °C with approximately

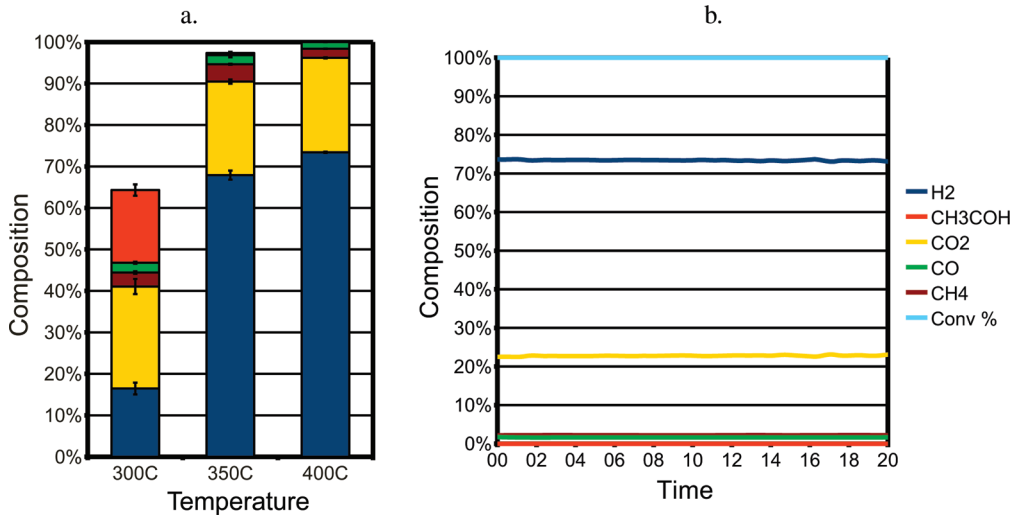

Figure 4. Untemplated catalyst results (10% Ni@CeO_2) showing 100% conversion at 400 °C and 12 000 h^{-1} GHSV. (a) Besides having 100% conversion, the amount of CO is comparable to the rhodium−nickel-based catalyst, and the amount of methane is significantly improved. (b) Stability testing of the nickel-only catalyst at 400 °C showing steady output over 20 h.

60% H_2, less than 0.5% CO, and no acetaldehyde in the product distribution, as shown in Figure S1a,b (Supporting Information). The best results in literature under similar conditions used Rh−Ni@CeO_2 and Co@CeO_2 catalysts with 90%+ ethanol conversion, but with 8−10% CO and 2−7% acetaldehyde in the product distribution, making the new catalysts preferable for use in fuel cells, where CO can act as a poison.[6,10,11] The untemplated and M13-templated catalyst showed similar product distributions under these conditions.

Increasing the GHSV from 12 000 to 36 000 h^{-1} at 300 °C by decreasing the amount of catalyst at the same input flow rate resulted in some decrease in activity accompanied by more CO and acetaldehyde with less CH_4, but ethanol conversion remained above 95%. Both catalysts show similar product distributions as shown in Figure S1c,d (Supporting Information). Samples without rhodium were also tested, as shown in Figure 4a,b. In the nickel-only samples, the activity of the 10% Ni@CeO_2 catalyst is particularly notable in that nickel alone on CeO_2 is achieving 100% ethanol conversion with an excellent product distribution, outperforming the mixed rhodium−nickel catalysts at 400 °C primarily due to the decrease in the amount of methane seen (8 to 2%) in the product distribution. Performance drops off quickly as temperature is decreased, demonstrating that the rhodium is necessary for low-temperature conversion. Conversion over the nickel-only catalyst was steady over 20 h, as shown in Figure 4b. The nickel-only catalyst performed more poorly when templated onto M13 than when left untemplated, as shown in Figure S1 (Supporting Information). This decreased performance suggests that impurities remaining from the biological material are contaminating the catalyst and reducing activity. For example, residual carbon, sulfur, phosphorus, or other biologically common elements may reduce the activity of the supported catalyst. This deactivation was not seen in the catalyst made with added rhodium.

In order to investigate the long-term thermal stability, catalysts were also tested at 450 °C and 120 000 h^{-1} GHSV by decreasing the amount of catalyst to 100 mg. Under these conditions, M13-templated catalysts showed near complete conversion (99−100% ethanol conversion) and steady performance over 52 h with 70% H_2 and about 5% CH_4, 3% CO, and 1% acetaldehyde in the product stream. At similar flow rates and temperatures, Rh−Ni@CeO_2 catalysts reported in literature showed complete conversion, but with 50% H_2 and 19% CH_4, while Co@CeO_2 catalysts produced 70% H_2, 9% CO, and 2% acetaldehyde.[6,10,11,15]

M13-templated catalyst showed improved thermal stability compared to untemplated catalyst through a combination of resistance to surface deactivation on rhodium and less phase segregation. While M13-templated catalyst showed steady output over a 52 h measurement, untemplated catalyst showed decreased conversion over time, as shown in Figure 5a−c. The decreased conversion is partially recovered by exposing the catalyst to air for a short time, indicating a surface deactivation most likely caused by carbon buildup.[39] However, a second 52 h measurement of the reactivated untemplated catalyst shows more rapid deactivation, indicating that the degradation of the catalyst is also caused by long-term effects. Nanowires were not tested a second time as they did not show noticeable deactivation over the first test.

XRD of the catalyst samples put on stream for stability tests shows that, in both cases, impurity phases begin to appear (Figure 5d,e). In the case of M13-templated catalyst, small NiO and Rh_2O_3 peaks are seen after a 52 h measurement at 450 °C and 120 000 h^{-1}

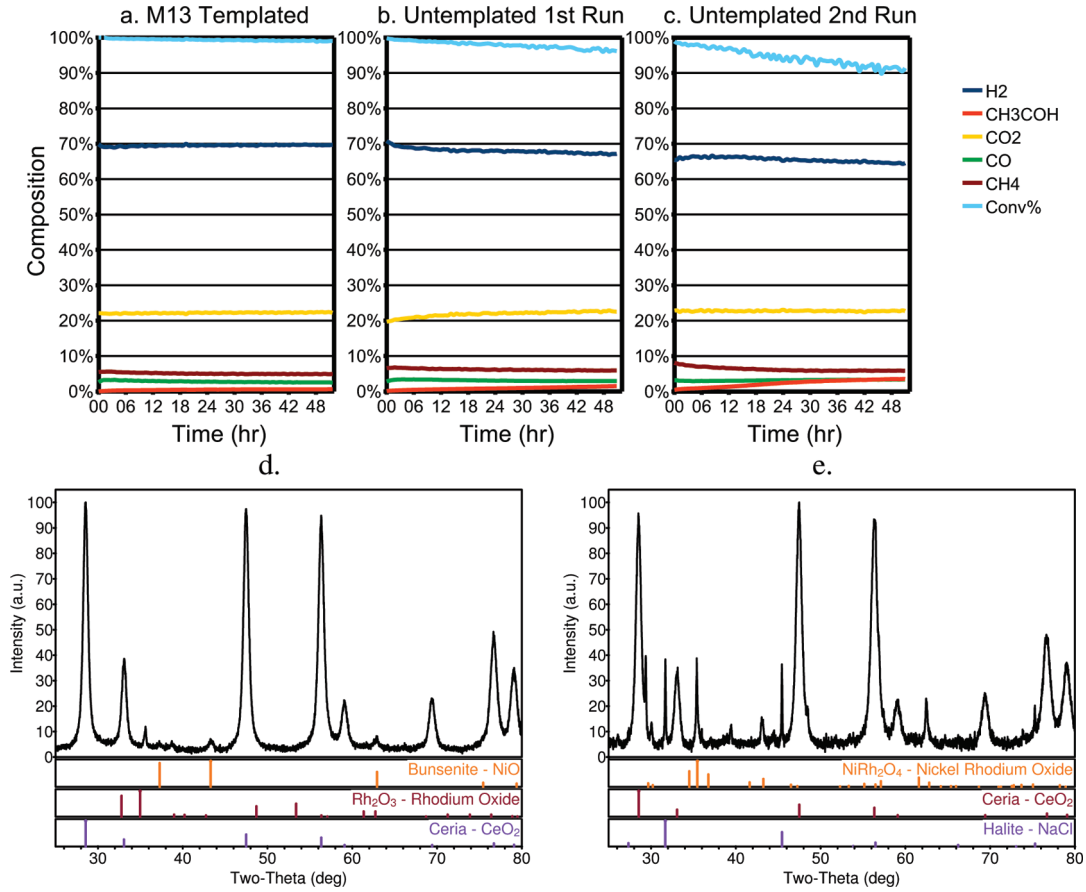

Figure 5. Long-term deactivation tests at 120 000 h^{-1} and 450 °C using 1% Rh/10% Ni@CeO_2. (a) With M13 templating, total conversion drops by only 1% over 52 h. (b) Untemplated catalyst shows total conversion dropping by 4% and decreased hydrogen in the product fraction over 52 h. (c) Faster deactivation is seen in a second 52 h test of untemplated catalyst after regeneration under air for 1 h, with total conversion dropping by 10%. (d) XRD of M13-templated catalyst after 52 h on stream. Peaks for NiO, Rh_2O_3, and CeO_2 are seen. (e) XRD of untemplated catalyst after two 52 h measurements with 1 h of regeneration under air. CeO_2 and NaCl peaks are seen, accompanied by Ni−Rh oxides. The double peak at 30° is characteristic of $NiRh_2O_4$.

GHSV. In the case of the untemplated sample, while NiO and Rh_2O_3 may be forming, a double peak at 30° suggests the formation of more complex mixed oxides such as $NiRh_2O_4$ after two 52 h measurements at 450 °C and 120 000 h^{-1} GHSV. On the basis of XRD peak broadening, the characteristic size of the NiO phases in the templated catalyst after 52 h on stream was ~14 nm, while the Rh_2O_3 phases were ~37 nm. In the untemplated sample after 105 h, the $NiRh_2O_4$ phase showed a characteristic size of ~52 nm. The more complex mixed nickel rhodium oxide phase is not seen in the M13-templated catalyst, suggesting that the extent to which nickel oxide and rhodium oxides mix to form mixed nickel rhodium oxides may play a role in the permanent deactivation of the catalyst over time.

To determine what role chlorine plays in the catalytic activity of this system, 1% Rh/10% Ni@CeO_2 was formed using cerium, rhodium, and nickel nitrate precursors. These particles performed poorly at 200 °C compared to the particles synthesized from chloride precursors. While untemplated 1% Rh/10% Ni@CeO_2 nanoparticles made from chloride precursors were still fairly active at 200 °C with 73% ethanol conversion, 1% Rh/10% Ni@CeO_2 catalysts made from nitrates only showed 45% ethanol conversion. The poor performance of the catalysts made using only nitrates suggests that the chlorine ions are playing a role in the activity.

We have shown in this work that, in the prototypical ethanol reforming reaction, catalysts formed by biotemplating onto the M13 bacteriophage have significantly different physical properties from catalysts of identical composition formed without the M13 bacteriophage. In particular, the M13 templating process improves long-term stability, reduces vulnerability to surface deactivation, and results in smaller pores with a narrower pore size distribution. Initial performance of both nanoparticles and nanowires was similar, and both nanoparticles and nanowires performed better than catalysts reported in literature to date. This makes the 1% Rh/10% Ni@CeO_2 catalyst a good choice in applications requiring either low temperatures or exceptional stability.

We have also demonstrated the ability of nickel alone on ceria to catalytically reform ethanol without the presence of rhodium at slightly higher tempera-

tures (400 °C), offering an alternative, inexpensive catalyst when higher temperatures are acceptable. Overall, we suggest that, if cost is the primary process design constraint, the use of 10% Ni@CeO_2 without M13 is an excellent choice. However, if the primary process design constraint is low temperature or long-term stability, the 1% Rh/10% Ni@CeO_2 M13-templated catalyst is a good alternative.

EXPERIMENTAL SECTION

Ni−Rh@CeO_2 was formed by using the oxidation and hydrolysis of $CeCl_3$ with $RhCl_3$ and $NiCl_2$ in aqueous solution. Water (120 mL) was either used as-is or by diluting E3M13 phage (AEEE expressed on the pVIII major coat protein) to a concentration of approximately 10^{12}/mL by adding ~10−100 μL of phage solution at a spectroscopically measured approximate concentration of ~10^{15}/mL. The diluted phage or phage-free water was mixed for 30 min in a 500 mL Ehrlenmyer flask at room temperature to ensure good dispersion. For comparison of different phage concentrations, the concentrated phage was decreased in concentration serially by factors of 10 to achieve an internally accurate phage ratio.

After mixing, 30 mL of 1 M metal chloride solution containing $RhCl_3$ (anhydrous, 99.9% Alfa Aesar), $NiCl_2$ (anhydrous, 98% Alfa Aesar), and $CeCl_3$ (heptahydrate, 99% Acros Organics) in a 1:10:89 molar ratio ($RhCl_3$/$NiCl_2$/$CeCl_3$) was added to either diluted M13 phage or phage-free water and allowed to equilibrate over 30 min at room temperature at 650 rpm.

After equilibration, nanoparticles were nucleated by the rapid addition of a mixture of 30 mL of 3 M NaOH (99%, Mallinckrodt Chemicals) and 60 μL of 30 wt % H_2O_2 (29.0−32.0% Reagent ACS, VWR). Immediately after addition, the solution turned dark brown-red and solids formed with gas evolution. The solution was stirred at 650 rpm for 30 min to allow the reaction to go to completion. After completion, the suspension was precipitated using centrifugation and the supernatant discarded. The precipitate was redissolved in water to wash residual NaCl and NaOH from the powder and recentrifuged for a total of three washings. After washing, the precipitate was set out at room temperature in a Petri dish in air until dry. After drying, the powders were finely ground and heat treated at 400 °C for 2 h until the final powder was produced. TGA on similar samples show that 350 °C is a sufficiently high temperature to remove nearly all of the carbon from the sample.[38]

Catalyst powders were loaded in an unpacked layer in a 316 stainless steel chamber (Swagelok Part SS-4F-05 In-Line Particulate Filter) (Figure S6f, Supporting Information) where the filter element was replaced with a 12 mm fine porosity fritted borosilicate disk (ChemGlass Part CG-201-05) to a typical depth of ~5 mm in the case of 1000 mg samples. In the case of very small samples (100 mg), a thin layer was placed on the borosilicate disk by gently tapping the catalyst chamber until the disk was no longer visible. The disk was replaced after each test, and the gas-hourly space velocity (GHSV) was changed by using varying amounts of catalyst powder while keeping the absolute flow rate constant to eliminate variations due to reactor activity or pressure changes due to increased flow rate. The GHSV was estimated by using an assumed catalyst density of 1 g/mL, and the gas volume was converted to a standard volume at 298 K and 1 atm.

The entire catalyst chamber was heated to the desired reaction temperature using a tube furnace (HTF55122A 1-Zone 1200 °C furnace with CC58114COMA-1 Digital Controller, Thermo Fisher Scientific) (Figure S6e, Supporting Information). The preheating chamber was made out of 1 in. diameter 316 stainless steel tubing with custom machined Swagelok fittings (Figure S6d,k, Supporting Information) to allow for the fuel injector (16 lb/h disc high-Z fuel injector, Racetronix Model 621040) (Figure S6b,j, Supporting Information) to inject liquid directly into the preheating chamber. The fuel injector temperature was measured using a thermocouple on the Swagelok fitting and heated with heat tape (McMASTER-CARR Part 4550T12) wrapped around the preheating chamber outside of the furnace controlled using a temperature controller (Omega CNI3233-C24) to 120 °C.

The air mass flow controller in all experiments is set at 14 mL/min (2.94 mL/min O_2), argon flow controller was set at approximately 100 mL/min, and ethanol was injected with the fuel injector using a 1.157 ms pulse every 2 s at 50 psi and 24 VDC. This pulse length is equivalent to 2.91 μL per pulse based on fuel injector calibrations done by injecting known pulse lengths and counting the number of pulses required to inject 10 mL of liquid. The total molar ratio at STP for these amounts is 1.7:1:10:11 (air/EtOH/water/argon) with a total flow rate of roughly 200 mL/min.

The internal temperature of the preheating chamber was monitored using a temperature probe placed just above the catalyst bed (Figure S6a, Supporting Information) with a temperature controller (Omega CNI3233-C24), and the temperature of the input gas was typically close to the temperature of the furnace. The preheating chamber had two 1/8 in. Swagelok fittings (Figure S6c,l, Supporting Information) to allow for argon and air to be added to the mixture using a mass flow controller (Alicat MC-1 SLPM-D/5 M 0-1 SLPM) for the air and a manual flow controller for the argon backflow gas.

Below the reactor bed, the gas mixture was allowed to equilibrate in a 150 mL double-ended 316 stainless steel sample cylinder (Swagelok Part 316 L-50DF4-150) placed inside the furnace to prevent condensation (Figure S6g, Supporting Information). This volume represents a time to equilibration of roughly 7.5 min assuming approximately 10 times the replacement time to fully equilibrate at a new composition. The output gas is carried through a 0.5 μm 316 stainless steel filter (Swagelok Part SS-4FWS-05) (Figure S6h,m, Supporting Information) to the GC *via* 1/8 in. 316 stainless steel tubing sheathed in 1/4 in. copper tubing wrapped with high-temperature heat rope (McMASTER-CARR Part 3641K26) (Figure S6i,n, Supporting Information) and using a temperature controller (Omega CNI3233-C24) set to 120 °C to prevent condensation. The tubing enters the GC (Figure S6o, Supporting Information) through a valve with a 250 μL sample loop (Figure S6p, Supporting Information) held at 150 °C after passing through another 0.5 μm 316 stainless steel filter (Swagelok Part SS-2F-05) (Figure S6q, Supporting Information) to prevent clogs in the GC valves. The equilibrated composition is fed continuously through an Agilent 7890A gas chromatographer (Figure S6r, Supporting Information), where the sample loop is switched onto the column every 35 min.

The sample is measured by the GC initially configured to Agilent Configuration 7890-0047, which meets ASTM D3612A specifications, with modified inlet temperature to avoid water condensation (150 °C) and lengthened total run time to avoid overlap with any present higher molecular weight hydrocarbons. This configuration uses an argon background with a flame ionization detector (FID) and a nickel methanizing catalyst for the detection of hydrocarbons, CO_2, and CO, and a thermal conductivity detector (TCD) for the detection of H_2, O_2, N_2, and H_2O.

The results were calibrated using custom mixed gas calibrations provided by Airgas. Hydrogen was calibrated to 6.063% H_2 in argon, and 10 samples had a standard deviation of 0.051%. Carbon monoxide was calibrated to 9.568% CO in N_2, and 10 samples had a standard deviation of 0.023%. Methane was calibrated to 20.000% CH_4 in N_2, and 10 samples had a standard deviation of 0.035%. CO_2, O_2, and N_2 were calibrated using dry air. Water was calibrated by using a target 1:1 ratio injected and vaporized in the reactor with air for 10 measurements with the total sum of products forced to 100%. This closed to a water amount of 47.85% with a standard deviation of 0.76% over 10 samples. Ethanol and acetaldehyde were calibrated by mixing with water to a known molar ratio and calibrating by liquid injection of the diluted sample and comparison to the water amount measured to avoid any homogeneous decomposition arising

from flow through the reactor. Sample amounts are calculated from calibrations by measuring the area of the peaks and comparing to the areas of peaks at the calibration composition.

Bar graphs showing product distribution and activity are made by scaling the product distribution such that the total height is the total ethanol conversion while the internal product distribution is represented by the relative size of each component. Error bars are calculated by using the standard deviation of each scaled component amount over the 36 measurements, scaled proportionally by the amount each component is scaled. For each component, this error is estimated as

$$\sigma_A^{total} = \sqrt{(\sigma_A F)^2 + (\sigma_F A)^2} \quad (6)$$

where A is the fraction of total products for component A, σ_A is the standard deviation in the fraction of total products for component A over the 36 measurements, F is the total ethanol conversion percent, and σ_F is the standard deviation of the ethanol conversion percent over the 36 measurements.

Homogeneous decomposition was measured by injecting a 1:10 ethanol/water mixture into the reactor with no catalyst present. At 300 °C, homogeneous decomposition showed 18.5% conversion of ethanol to acetaldehyde estimated as the ratio of measured acetaldehyde to the sum of the measured acetaldehyde and measured ethanol. Essentially no H_2 or CH_4 was measured. Catalysis is likely taking place in the tubing, which contains nickel, and on the stainless steel filter elements, so by placing the catalyst powder as early as possible in the flow path, subsequent dehydrogenation is limited.

XRD crystallite sizes were determined by using the *in situ* furnace attachment for the PANalytical X'Pert PRO diffractometer with the X'Celerator detector and a Cu Kα source. Spectra were analyzed using Jade software, and the peak width was used to calculate average nanocrystallite size by fitting each peak to a Pearson-VII curve with no skewness.

TEM images were taken using a JEOL 2010 electron microscope at 200 keV. EDS was done using a GATAN detector in STEM mode on a JEOL 2010F with a field emission gun. BET data were collected using the Micromeritics ASAP 2020, and pore size distributions were estimated by using Micromeritics DFT Plus software with the original density functional theory model, with N_2 at 77 K on carbon with slit pores.

Acknowledgment. This work was funded in part by the Army Research Office and the Massachusetts Institute of Technology. The authors thank the MIT Shared Experimental Facilities supported by the MRSEC Program of the National Science Foundation for use of TEM and XRD equipment, the Institute for Soldier Nanotechnologies for use of BET equipment, and the MIT Edgerton Center for use of machining equipment.

Note added after ASAP Publication: An incorrect version of Figure 4a was posted on June 7, 2010. The correct version published on June 22, 2010.

Supporting Information Available: Complete catalyst selectivity and activity data for both templated and untemplated catalysts at varying flow rates, temperatures, and compositions, BET of catalyst materials, XRD characterization before and after offstream heat treatment, photos of reactor design, and TEM EDS data. This material is available free of charge *via* the Internet at http://pubs.acs.org.

REFERENCES AND NOTES

1. U.S. Department of Energy Hydrogen Program, *Comparison of Fuel Cell Technologies*; Technical Report, **2008**.
2. *CRC Handbook of Chemistry and Physics*, 90th ed.; Lide, D. R., Ed.; CRC Press: Boca Raton, FL, 2010.
3. Deluga, G. A.; Salge, J. R.; Schmidt, L. D.; Verykios, X. E. Renewable Hydrogen from Ethanol by Autothermal Reforming. *Science* **2004**, *303*, 993.
4. Salge, J. R.; Deluga, G. A.; Schmidt, L. D. Catalytic Partial Oxidation of Ethanol over Noble Metal Catalysts. *J. Catal.* **2005**, *235*, 69–78.
5. Zerva, C.; Philippopoulos, C. J. Ceria Catalysts for Water Gas Shift Reaction: Influence of Preparation Method on Their Activity. *Appl. Catal. B* **2006**, *67*, 105–112.
6. Kugai, J.; Subramani, V.; Song, C.; Engelhard, M. H.; Chin, Y.-H. Effects of Nanocrystalline CeO_2 Supports on the Properties and Performance of Ni-Rh Bimetallic Catalyst for Oxidative Steam Reforming of Ethanol. *J. Catal.* **2006**, *238*, 430–440.
7. Idriss, H. Ethanol Reactions over the Surfaces of Noble Metal/Cerium Oxide Catalysts. *Platinum Met. Rev.* **2004**, *48*, 105–115.
8. Sheng, P.-Y.; Yee, A.; Bowmaker, G. A.; Idriss, H. H_2 Production from Ethanol over Rh-Pt/CeO_2 Catalysts: The Role of Rh for the Efficient Dissociation of the Carbon−Carbon Bond. *J. Catal.* **2002**, *208*, 393–403.
9. Erdohelyi, A.; Rasko, J.; Kecskes, T.; Toth, M.; Domok, M.; Baan, K. Hydrogen Formation in Ethanol Reforming on Supported Noble Metal Catalysts. *Catal. Today* **2006**, *116*, 367–376.
10. Kugai, J.; Velu, S.; Song, C. Low-Temperature Reforming of Ethanol over CeO_2-Supported Ni−Rh Bimetallic Catalysts for Hydrogen Production. *Catal. Lett.* **2005**, *101*, 255.
11. Llorca, J.; Homs, N.; Sales, J.; de la Piscina, P. R. Efficient Production of Hydrogen over Supported Cobalt Catalysts from Ethanol Steam Reforming. *J. Catal.* **2002**, *209*, 306–317.
12. de Lima, S. M.; Colman, R.; Jacobs, G.; Davis, B. H.; Souza, K. R.; de Lima, A. F. F.; Appel, L. G.; Mattos, L. V.; Noronha, F. B. Hydrogen Production from Ethanol for PEM Fuel Cells. An Integrated Fuel Processor Comprising Ethanol Steam Reforming and Preferential Oxidation of Co. *Catal. Today* **2009**, *146*, 110–123.
13. Cai, W.; Wang, F.; Zhan, E.; Veen, A. C. V.; Mirodatos, C.; Shen, W. Hydrogen Production from Ethanol over Ir/CeO_2 Catalysts: A Comparitive Study of Steam Reforming, Partial Oxidation and Oxidative Steam Reforming. *J. Catal.* **2008**, *257*, 96–107.
14. Sheng, P. Y.; Chiu, W. W.; Yee, A.; Morrison, S. J.; Idriss, H. Hydrogen Production from Ethanol over Bimetallic Rh-M/CeO_2 (M = Pd or Pt). *Prepr. Pap.—Am. Chem. Soc., Div. Fuel Chem.* **2006**, *51*, 26.
15. Wang, H.; Ye, J. L.; Liu, Y.; Li, Y. D.; Qin, Y. N. Steam Reforming of Ethanol over Co_3O_4/CeO_2 Catalysts Prepared by Different Methods. *Catal. Today* **2007**, *129*, 305–312.
16. Pereira, E. B.; Homs, N.; Marti, S.; Fierro, J. L. G.; de la Piscina, P. R. Oxidative Steam-Reforming of Ethanol over Co/SiO_2, Co-Rh/SiO_2 and Co-Ru/SiO_2 Catalysts: Catalytic Behavior and Deactivation/Regeneration Processes. *J. Catal.* **2008**, *257*, 206–214.
17. Srisiriwat, N.; Therdthianwong, S.; Therdthianwong, A. Oxidative Steam Reforming of Ethanol over Ni/Al_2O_3 Catalysts Promoted by CeO_2, ZrO_2 and CeO_2-ZrO_2. *Int. J. Hydrogen Energy* **2009**, *34*, 2224–2234.
18. Iulianelli, A.; Longo, T.; Liguori, S.; Seelam, P. K.; Keiski, R. L.; Basile, A. Oxidative Steam Reforming of Ethanol over Ru-Al_2O_3 Catalyst in a Dense Pd−Ag Membrane Reactor To Produce Hydrogen for PEM Fuel Cells. *Int. J. Hydrogen Energy* **2009**, *34*, 8558–8565.
19. de Lima, S. M.; da Cruz, I. O.; Jacobs, G.; Davis, B. H.; Mattos, L. V.; Noronha, F. B. Steam Reforming, Partial Oxidation, and Oxidative Steam Reforming of Ethanol over Pt/$CeZrO_2$ Catalyst. *J. Catal.* **2008**, *257*, 356–368.
20. de Lima, S. M.; da Silva, A. M.; da Costa, L. O. O.; Graham, U. M.; Jacobs, G.; Davis, B. H.; Mattos, L. V.; Noronha, F. B. Study of Catalyst Deactivation and Reaction Mechanism of Steam Reforming, Partial Oxidation, and Oxidative Steam Reforming of Ethanol over Co/CeO_2 Catalyst. *J. Catal.* **2009**, *268*, 268–281.
21. Youn, M. H.; Seo, J. G.; Cho, K. M.; Park, S.; Park, D. R.; Jung, J. C.; Song, I. K. Hydrogen Production by Auto-Thermal Reforming of Ethanol over Nickel Catalysts Supported on

Ce-Modified Mesoporous Zirconia: Effect of Ce/Zr Molar Ratio. *Int. J. Hydrogen Energy* **2008**, *33*, 5052–5059.
22. Cai, W.; Wang, F.; Veen, A. C. V.; Provendier, H.; Mirodatos, C.; Shen, W. Autothermal Reforming of Ethanol for Hydrogen Production over an Rh/CeO_2 Catalyst. *Catal. Today* **2008**, *138*, 152–156.
23. Biswas, P.; Kunzru, D. Oxidative Steam Reforming of Ethanol Over Ni/CeO_2-ZrO_2 Catalyst. *Chem. Eng. J.* **2007**, *136*, 41–49.
24. Biswas, P.; Kunzru, D. Steam Reforming of Ethanol on Ni-CeO_2-ZrO_2 Catalysts: Effect of Doping with Copper, Cobalt and Calcium. *Catal. Lett.* **2007**, *118*, 36.
25. Wheeler, C.; Jhalani, A.; Klein, E. J.; Tummala, S.; Schmidt, L. D. The Water-Gas-Shift Reaction at Short Contact Times. *J. Catal.* **2004**, *223*, 191–199.
26. Houtman, C. J.; Barteau, M. A. Divergent Pathways of Acetaldehyde and Ethanol Decarbonylation on the Rh(111) Surface. *J. Catal.* **1991**, *130*, 528–546.
27. Yee, A.; Morrison, S. J.; Idriss, H. The Reactions of Ethanol over M/CeO_2 Catalysts. Evidence of Carbon−Carbon Bond Dissociation at Low Temperatures over Rh/CeO_2. *Catal. Today* **2000**, *63*, 327–335.
28. Deshpande, S.; Patil, S.; Kuchibhatla, S. V. N. T.; Seal, S. Size Dependency Variation in Lattice Parameter and Valency States in Nanocrystalline Cerium Oxide. *Appl. Phys. Lett.* **2005**, *87*, 133113.
29. Zhang, F.; Wang, P.; Koberstein, J.; Khalid, S.; Chan, S. W. Cerium Oxidation State in Ceria Nanoparticles Studied with X-ray Photoelectron Spectroscopy and Absorption Near Edge Spectroscopy. *Surf. Sci.* **2004**, *563*, 74–82.
30. Esch, F.; Fabris, S.; Zhou, L.; Montini, T.; Africh, C.; Fornasiero, P.; Comelli, G.; Rosei, R. Electron Localization Determines Defect Formation on Ceria Substrates. *Science* **2005**, *309*, 752.
31. *Catalysis by Ceria and Related Materials*; Trovarelli, A., Ed.; Imperial College Press: London, 2002.
32. Fu, Q.; Saltsburg, H.; Flytzani-Stepanopoulos, M. Active Nonmetallic Au and Pt Species on Ceria-Based Water-Gas Shift Catalysts. *Science* **2003**, *301*, 935.
33. Liu, Z.; Jenkins, S.; King, D. Origin and Activity of Oxidized Gold in Water-Gas-Shift Catalysis. *Phys. Rev. Lett.* **2005**, *94*, 196102.
34. Dutta, P.; Pal, S.; Seehra, M. S.; Shi, Y.; Eyring, E. M.; Ernst, R. D. Concentration of Ce^{3+} and Oxygen Vacancies in Cerium Oxide Nanoparticles. *Chem. Mater.* **2006**, *18*, 5144–5146.
35. Lee, Y. J.; Yi, H.; Kim, W.-J.; Kang, K.; Yun, D. S.; Strano, M. S.; Ceder, G.; Belcher, A. M. Fabricating Genetically Engineered High-Power Lithium-Ion Batteries Using Multiple Virus Genes. *Science* **2009**, *324*, 1051.
36. Nam, K. T.; Kim, D.-W.; Yoo, P. J.; Chiang, C. Y.; Meethong, N.; Hammond, P. T.; Chiang, Y. M.; Belcher, A. M. Virus-Enabled Synthesis and Assembly of Nanowires for Lithium Ion Battery Electrodes. *Science* **2006**, *312*, 885.
37. Nam, K. T.; Wartena, R.; Yoo, P. J.; Liau, F. W.; Lee, Y. J.; Chiang, Y.-M.; Hammond, P. T.; Belcher, A. M. Stamped Microbattery Electrodes Based on Self-Assembled M13 Viruses. *Proc. Natl. Acad. Sci. U.S.A.* **2008**, *105*, 17227–17231.
38. Mao, C.; Solis, D.; Reiss, B.; Kottman, S.; Sweeney, R.; Georgiou, G.; Iverson, B.; Belcher, A. Virus-Based Genetic Toolkit for the Directed Synthesis of Magnetic and Semiconducting Nanowires. *Science* **2004**, *303*, 213–215.
39. Wang, H.; Liu, Y.; Wang, L.; Qin, Y. N. Study on the Carbon Deposition in Steam Reforming of Ethanol over Co/CeO_2 Catalyst. *Chem. Eng. J.* **2008**, *145*, 25–31.